Nonlinear alignment between conical emissions generated in a four-wave parametric mixing process

A. Dreischuh[2], **U. Reiter-Domiaty**[1], **D. Gruber**[1], **L. Windholz**[1], **S. Dinev**[2]

[1] Technische Universität Graz, Institut für Experimentalphysik, Petersgasse 16, A-8010 Graz, Austria
(FAX: +43-316/873 86 55, E-mail: reiter@fexphal01.tu-graz.ac.at)
[2] Sofia University, Department of Quantum Electronics, 5 J. Bourchier Blvd., BG-1164 Sofia, Bulgaria
(FAX: +359-2/962 52 76, E-mail: aldrei@phys.uni-sofia.bg)

Abstract. The dependence of the yellow conical emission angle on pump laser intensity is studied experimentally in dense Na vapor under near-resonant one-photon excitation of the sodium 4^2P levels. A numerical model developed to describe mechanisms involved in the conical emission generation processes indicates that the saturation observed is due to the opposite angular tuning of the near-infrared and yellow conical emission generated in the same process. The mechanisms responsible are assigned to (self)induced phase modulation processes of the waves involved.

PACS: 42.65; 42.65 k; 51.70

Conical Emission (CE) arising from dense atomic vapor associated with (near) resonant propagation of an intense laser field through a nonlinear medium has been studied by many authors over the last two decades (e.g. [1–14]). Following the classification of investigations of CE by Pender et al. [7], we present a study of CE generated in a Four-Wave Parametric Mixing (FWPM) process induced by one-photon pumping of the second resonant transitions in Na vapor.

The intense laser beam, propagating through the sodium vapor causes the refractive index of the nonlinear medium to be changed. This can modify the phase, amplitude and frequency of the pump wave, resulting in pump Self-Phase Modulation (SPM) [15]. If weak optical waves (e.g. the signal wave in an FWPM-process) are influenced by the intense field in the nonlinear medium, "Induced Phase Modulation" (IPM) can be expected [16]. IPM between copropagating optical waves are assigned to Cross-Phase Modulation (XPM) [17]. In an FWPM process both SPM and IPM/XPM can influence the phase-matching conditions and thus change the process efficiency [18, 19]. In the particular case of a Raman-resonant FWPM we found that the non-monotonically tuning with laser frequency of the CE generated in Na vapor can be explained by a model in which the resonant-enhanced SPM and IPM does not disturb the linear (here "linear" means linear with respect to the intensity) vector synchronism of the process [20]. Recently, nonlinear self-phase matching in an

initially nonphase matched second harmonic generation process was observed by S. Orlov et al. [21] leading to a pattern formation in the structure of the generated beam.

In this work we present a systematical study of experimental results describing the dependance of the CE angle on the pump laser intensity. The theoretical model developed within our investigations provides insight into the mechanisms involved.
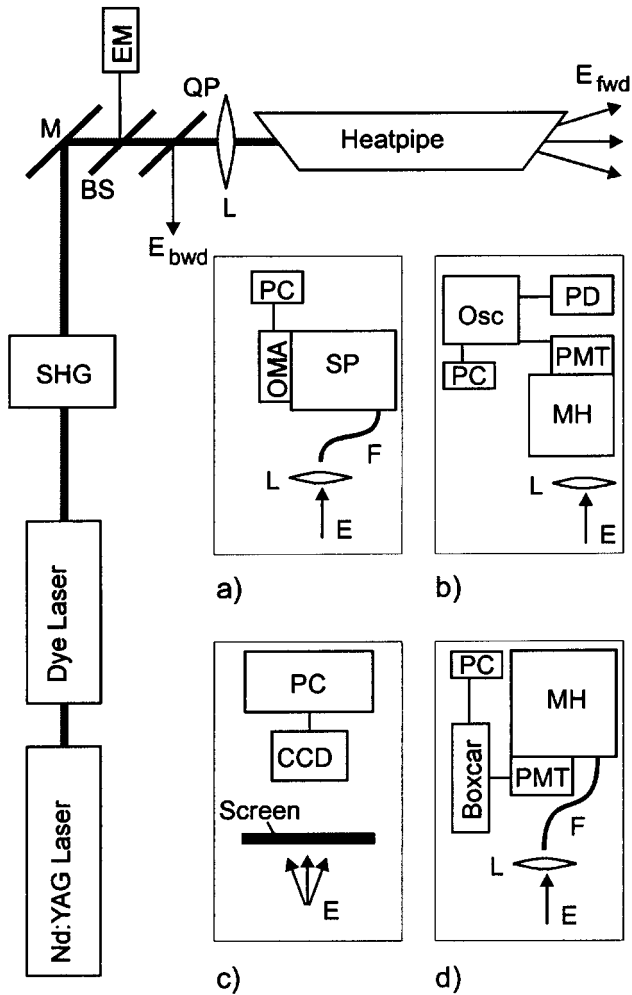
1 Experimental setup and results

The experimental setup is shown in Fig. 1. Sodium vapor was contained in a heat pipe oven with a 6 cm heated zone. During experiments vapor pressure density, calculated from temperature (300–500 °C) was changed in the range $N \approx 10^{15} – 2 \times 10^{17}$ cm^{-3}. Argon was added as buffer gas with typical pressures of 55–65 mbar.

Sodium vapor was excited near the Na(3^2S–4^2P) single photon resonances (see Fig. 2) by the focused second harmonic of a dye laser (Radiant Dyes DL Midi, operated with DCM), pumped by the 532 nm output of an Nd:YAG laser (Quanta Ray GCR 170). The pulse energy was about 4 mJ with typical pulse duration of 8 ns, spectral line width of 0.01 nm and a repetition rate of 10 Hz. The excitation wavelength was scanned continuously by angle tuning of a KDP doubling crystal, following grating tuning of the dye laser under computer control. The laser pulse energy was continuously monitored by an energy meter.

Na emissions emerging from the heat pipe were focused on an optical fiber and spectrally resolved by a 50 cm triple grating monochromator/spectrograph (Acton) equipped with 150, 600, and 1200 grooves/mm gratings. The corresponding range of wavelengths was imaged on a gateable intensified 1024 diode array of an OMA optical multichannel analyzer cooled to −25 °C. A high voltage pulse generator allowed time resolved spectral measurements. The Nd:YAG pump laser and the diode array were synchronized by the OMA control unit and the pulse generator.

Emission spectra were recorded by averaging the output signal over a certain number of pulses using the exposure time
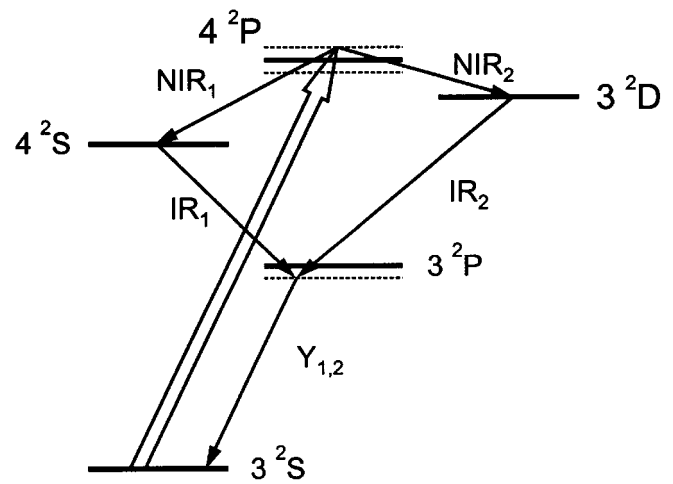
Fig. 1. Experimental setup. **a** Measurements of forward and backward emission from laser excited sodium vapor by an optical multichannel analyzer system. **b** Measurements of the time behavior of the emissions by a monochromator–photomultiplier detection system. **c** Investigations of the spatial features of the emissions by a CCD camera. **d** Measurements of forwards and backwards directed emissions by scanning the monochromator and by means of a boxcar averager detection system. (SHG second harmonic generation, M Mirror, BS beam splitter, QP quartz plate, L lens, EM energy meter, F optical fiber, SP spectrograph, OMA optical multichannel analyzer system, PC personal computer, MH monochromator, PMT photomultiplier, Osc fast storage oscilloscope, PD fast photodiode for detecting the time behavior of the laser pulse, CCD camera, E emission)

Fig. 2. Simplified diagram of the Na states involved in the FWPM process leading to the generation of a conical emission. NIR emission in the infrared, IR emission in the near infrared, Y yellow emission. The indices refer to the two possible cascades

of OMA and stored to an additional computer for further analysis. Backward scattered emission was measured by placing an uncoated quartz plate under $45°$ in front of the heat pipe oven.

A Hamamatsu R-955 photomultiplier with a rise time of 2.2 ns coupled to the monochromator output, in conjunction with a LeCroy 600 MHz digital storage oscilloscope was used to measure the temporal evolution of individual spectral components. The trigger signal was provided by a fast photodiode with a rise time of 1 ns. The oscilloscope data were stored to a computer using a GPIB interface. A sodium spectral lamp was used for wavelength calibration.

The spatial distribution of the emitted radiation was investigated by use of a CCD color video camera recording the emission evolution as a function of excitation wavelength, vapor density, pump energy, and pump-beam diameter. Emis-

sion profiles were digitized by a frame grabber and stored to a DEC 3800 work station for further analysis. Further investigations of the spatial distribution of radiation have been performed by moving the optical fiber coupled to the OMA spectrograph step by step across the output beam in a plain located 69 cm from the heat pipe output, recording spectra at each step.

In Fig. 3 experimental values of the yellow CE half angle are presented in dependence of the dye-laser intensity at a pump-wavelength $\lambda_L = 330.13$ nm. At Na densities of $N = 1.6 \times 10^{17}$ cm^{-3} the center of gravity wavelength of the broadband CE generated was $\lambda_Y = 589.9$ nm. Within an experimental accuracy of 0.02 nm, λ_Y was found to be independent of the pump-laser intensity. As seen in Fig. 3, the initial rapid increase in the CE angle is followed by a well-pronounced saturation up to laser intensities of 2×10^9 W/cm^2. (The maximum pump intensity used within our investigation was about 10^{10} W/cm^2.) Qualitatively the
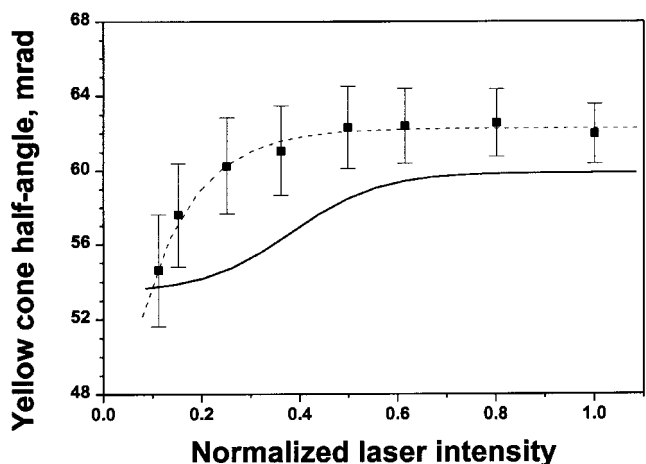
Fig. 3. Dependence of the yellow conical emission half-angle on the pump laser intensity at $\lambda_L = 330.13$ nm, $\lambda_Y = 589.9$ nm and $N = 1.6 \times 10^{17}$ cm^{-3}. *Squares* experimental data, the run is indicated by a *dashed line*; solid curve numerical result. Full laser intensity 2×10^9 W/cm^2

same behavior was observed at a laser excitation wavelength of $\lambda_L = 332.33$ nm and Na densities of $N = 2.8 \times 10^{16}$ cm^{-3} (Fig. 4).

The dashed curves in Figs. 3 and 4 are fits of the experimental data, whereas the solid lines represent the numerical results obtained within our investigations (see Sect. 2).

2 Numerical model

In order to get a more detailed description of the process observed, we developed a model based on a system of coupled nonlinear equations [7] describing the FWPM in both, the $3S - 4P - 4S - 3P$ and $3S - 4P - 3D - 3P$ cascades. For convenience of notation the transition $4^2S - 3^2P$ is denoted as IR$_1$ in Fig. 2, although the corresponding wavelength (1.13 μm) belongs to the near-infrared spectral range. For the sake of clarity we first present the model equations for the $3S - 4P - 4S - 3P$ cascade which are

$$\frac{dE_L}{dz} = -\frac{\alpha_L}{2}E_L - i\gamma_{SPM}^L \frac{|E_L|^2}{2}E_L - i\Gamma_{eff}^L E_L$$
$$- i\sum_{j=1}^{2} \gamma_{FWPM}^{(j)} E_{NIR_j} E_{IR_j} E_{Y_j} \exp\left\{-i\Delta k_j z\right\} \quad (1a)$$

$$\frac{dE_{NIR_1}}{dz} = -\frac{\alpha_{NIR_1}}{2}E_{NIR_1} - i\gamma_{IPM}^{NIR_1,L}|E_L|^2 E_{NIR_1}$$
$$- i\gamma_{FWPM}^{(1)} E_L E_{IR_1}^* E_{Y_1}^* \exp\left\{-i\Delta k_1 z\right\} \quad (1b)$$

$$\frac{dE_{IR_1}}{dz} = -\frac{\alpha_{IR_1}}{2}E_{IR_1} - i\Gamma_{eff}^{IR_1} E_{IR_1}$$
$$- i\gamma_{FWPM}^{(1)} E_L E_{NIR_1}^* E_{Y_1}^* \exp\left\{-i\Delta k_1 z\right\} \quad (1c)$$

$$\frac{dE_{Y_1}}{dz} = -\frac{\alpha_{Y_1}}{2}E_{Y_1} - i\gamma_{SPM}^{Y_1}|E_{Y_1}|^2 E_{Y_1} - i\Gamma_{eff}^{Y_1} E_{Y_1}$$
$$- i\gamma_{FWPM}^{(1)} E_L E_{NIR_1}^* E_{IR_1}^* \exp\left\{-i\Delta k_1 z\right\} \quad (1d)$$

where

$$\Gamma_{eff}^L = \sum_{j=1}^{2} \gamma_{IPM}^{L,NIR}|E_{NIR_j}|^2 + \gamma_{IPM}^{L,Y_j}|E_{Y_j}|^2 \quad (2a)$$

$$\Gamma_{eff}^{IR_1} = \gamma_{IPM}^{IR_1,Y_1}|E_{Y_1}|^2 + \gamma_{IPM}^{L,Y_2}|E_{Y_2}|^2 \quad (2b)$$

and

$$\Gamma_{eff}^{Y_1} = \sum_{j=1}^{2} \gamma_{IPM}^{Y_1,j}|E_j|^2 \quad (j = L, Y_2, R_1, R_2) \quad (2c)$$

denote the effective nonlinearities due to the IPM. In (1a)–(1d) E_L, E_{NIR_j}, E_{IR_1} and E_{Y_1} are the slowly-varying field amplitudes of the laser, the near-infrared ($4^2P - 4^2S$), the infrared and the yellow waves, respectively. The remaining three equations for the $3S - 4P - 3D - 3P$ cascade can be obtained from (1b)–(1d) by substituting the sub/superscripts "1" by "2". The same holds for the effective nonlinearities described by (2a)–(2c). Since time-integrated CE spatial distribution was recorded in the experiment and nanosecond pulses were used, the time-coordinate was treated as a parameter and we integrated numerically over 100 CE time profiles (50 of them within the pulse full width at half maximum). In the model equations α_k represents absorption coefficients, $\gamma_i^{j,k}$ the nonlinear refractive-index coefficients due to SPM/IPM (index i) of the j-th wave originating from the k-th wave, and Δk_i the projection of the wave-vector mismatch $\Delta k = k_L - (k_{NIR_i} + k_{IR_i} + k_{Y_i})$ on the axis of the pump (see also Fig. 5).

Since the CE is generated under conditions under which both, energy and momentum are conserved, a closed (perfectly phase-matched) vector diagram results in yellow CEs angular offset at the angles

$$\beta_i^{off} = \arccos\left\{\left[|k_L| - |k_{NIR_i}| - |k_{IR_i}|/|k_{Y_i}|\right]\right\}, \quad i = 1, 2 \quad (3a)$$

with respect to the axis of the laser pump beam (see Fig. 5), assuming, that the Stokes emission (λ_{NIR}) is amplified collinear with the pump wave along its propagation axes. Therefore, the infrared waves IR$_1$ and IR$_2$ should emerge from the sodium vapor on a conical shell. Their angular offsets can be described by the relation

$$\alpha_i^{off} = \arccos\left\{1 - \left(\frac{|k_{Y_i}|}{|k_{IR_i}|}\right)^2 \sin^2\left(\beta_i^{off}\right)\right\}^{1/2} \quad (3b)$$

Therefore, the wave-vector mismatch Δk_i for the i-th cascade takes the form

$$\Delta k_i = k_{IR_i}\left\{\sqrt{1 - \left(\frac{k_{Y_i}}{k_{IR_i}}\right)^2 \sin^2\left(\beta - \beta_i^{off}\right)} - 1\right\}$$
$$+ k_{Y_i}\left[\cos\left(\beta - \beta_i^{off}\right)\right] \quad i = 1, 2 \quad (4)$$

where β is the angular coordinate with respect to the axis of the pump beam. Obviously, $\beta = \beta_i^{off}$ corresponds to
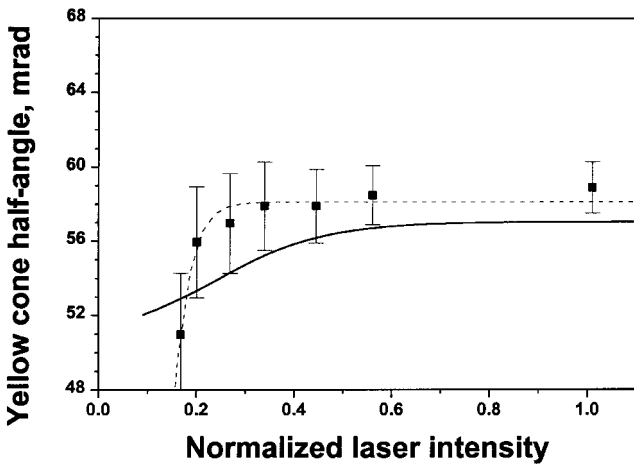

Fig. 4. The same as in Fig. 3 at $\lambda_L = 332.33$ nm, $\lambda_Y = 591.9$ nm and $N = 2.8 \times 10^{16}$ cm^{-3}. Full laser intensity 10^{10} W/cm^2
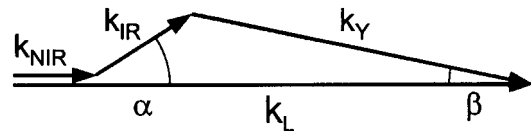

Fig. 5. Wave-vector diagram for an FWPM in one of the cascades involved in the model (β–yellow CE half angle; α–CE half angle for the infrared emission)

$\Delta k = 0$, i.e. to a perfect phase-matching and optimum conversion efficiency under plane-wave conditions. The presence of a focusing lens in front of the heat pipe (see Introduction) is taken into account in our model study by introducing a convergence of the pump beam resulting in a linear beam-waist of the length equal to the sodium column length in the heat pipe (6 cm). This approach implies that the pump has a Gaussian beam-profile. In order to keep during the experiments the beam profile unchanged while varying the pulse energy, the laser output was set to a maximum of energy and was reduced before entering the heat pipe oven by neutral density filters.

3 Discussion

All parameters used in the numerical simulation of the CE generation are summarized in Table 1. Because of the branching ratio between the cascade emissions (Fig. 2), we found

Table 1. Parameters used in the model calculations

Parameter	Unit	Value ($\lambda_L = 330.13$ nm)	Value ($\lambda_L = 332.35$ nm)
λ_{NIR1}	nm	2196.43	2299.54
λ_{R1}	nm	1137.92	1130.18
λ_{Y1}	nm	589.9	591.9
λ_{NIR2}	nm	8936.43	10919.3
λ_{IR2}	nm	818.26	814.26
λ_{Y2}	nm	589.9	592.1
N	cm^{-3}	1.6×10^{17}	1.8×10^{16}
α_L	cm^{-1}	$2.3 \times 10^{-17} N$	$1.6 \times 10^{-19} N$
α_{NIR1}	cm^{-1}	$1.2 \times 10^{-15} N$	$4.5 \times 10^{-18} N$
α_{R1}	cm^{-1}	$9 \times 10^{-15} N$	$2.4 \times 10^{-17} N$
α_{Y1}	cm^{-1}	$6 \times 10^{-15} N$	$1.5 \times 10^{-17} N$
α_{NIR2}	cm^{-1}	$4 \times 10^{-16} N$	$4.5 \times 10^{-18} N$
α_{IR2}	cm^{-1}	$4.5 \times 10^{-14} N$	$1.3 \times 10^{-16} N$
α_{Y2}	cm^{-1}	$6 \times 10^{-15} N$	$1.3 \times 10^{-16} N$
$[n(\lambda_L - 1)]/N$	cm^3	-7.7×10^{-22}	-2.1×10^{-22}
$[n(\lambda_{NIR1} - 1)]/N$	cm^3	-3.2×10^{-19}	3.8×10^{-20}
$[n(\lambda_{IR1} - 1)]/N$	cm^3	-1.2×10^{-19}	-1.5×10^{-20}
$[n(\lambda_{Y1} - 1)]/N$	cm^3	1.5×10^{-19}	1.7×10^{-20}
$[n(\lambda_{NIR2} - 1)]/N$	cm^3	-2.2×10^{-19}	4.7×10^{-20}
$[n(\lambda_{R2} - 1)]/N$	cm^3	-1.5×10^{-19}	-4.3×10^{-20}
$[n(\lambda_{Y2} - 1)]/N$	cm^3	1.5×10^{-19}	1.6×10^{-20}
I_L	W/cm^2	10^8–2×10^9	10^{10}
γ_{SPM}^L	esu	8×10^{-31}	6.5×10^{-33}
γ_{SPM}^{Y1}	esu	-1.2×10^{-28}	-3.3×10^{-31}
γ_{SPM}^{Y2}	esu	-1.2×10^{-28}	-3.9×10^{-31}
$\gamma_{IPM}^{NIR2,L}$	esu	-6.2×10^{-35}	-1.2×10^{-36}
$\gamma_{IPM}^{NIR1,L}$	esu	-6.3×10^{-35}	-1.2×10^{-36}
$\gamma_{IPM}^{Y1,L}$	esu	1.5×10^{-30}	2.9×10^{-32}
$\gamma_{IPM}^{Y2,L}$	esu	1.5×10^{-30}	3.4×10^{-32}
$\gamma_{IPM}^{Y1,Y2}$	esu	-2×10^{-28}	-1.5×10^{-29}
$\gamma_{IPM}^{Y1,IR1}$	esu	-4.4×10^{-30}	-1.1×10^{-31}
$\gamma_{IPM}^{Y1,IR2}$	esu	-3.2×10^{-30}	-1.5×10^{-31}
$\gamma_{IPM}^{Y2,IR2}$	esu	-3.2×10^{-30}	-1.3×10^{-31}
$\gamma_{IPM}^{Y2,IR1}$	esu	-4.4×10^{-30}	-8.5×10^{-31}
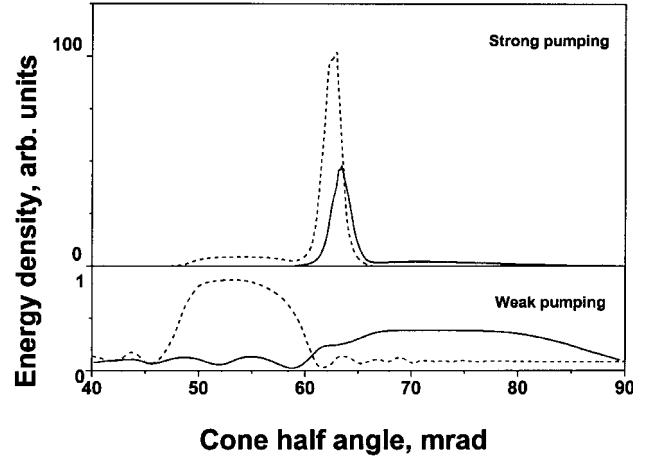
Fig. 6. Energy density of the yellow (*dashed* curve) and infrared (*solid*) CE under weak (2×10^8 W/cm^2) and strong (2×10^9 W/cm^2) pumping of the 4^2P state of Na ($\lambda_L = 330.13$ nm, $N = 1.6 \times 10^{17}$ cm^{-3})

that in the FWPM observed, the $4^2P - 4^2S - 3^2P - 3^2S$ cascade dominates the processes, but nevertheless the numerical results are calculated by solving the complete system of equations by means of the Runge–Kutta method. The step width was chosen to perceive the calculation accuracy.

The nonlinear coefficients $\gamma_i^{j,k}$ related to the third-order nonlinear susceptibilities $\chi_i^{j,k}$ are calculated from the Feynman diagram formalism [22] with an accuracy of 40%, according to that of the dipole matrix elements [23]. The values of refractive indices are obtained from the Sellmayer equation [24] taking the pressure broadening of the Na atomic lines at the particular vapor densities into consideration. Nonlinear model coefficients for the FWPM process are estimated to be $|\gamma_{FWM}^{(1)}| = 10^{-29}$ esu at $\lambda_L = 330.13$ nm and $|\gamma_{FWM}^{(1)}| = 5 \times 10^{-32}$ esu at $\lambda_L = 332.33$ nm.

The laser and yellow emission SPM and the IPM strongly influence CE generation. Although the nonlinearities for XPM between the yellow and the infrared waves are quite high, their influence could be expected to be less because of the reduced overlapping between the corresponding CEs.

The solid curves in Figs. 3 and 4 present numerical results obtained in simulating the CE generation via FWPM by single-photon pumping of the second resonance transition of the Na atoms. After a rapid growing of the CE angle with laser intensity, saturation of yellow CE can be observed and seems to be well expressed. The difference between calculated and measured CE half-angle can be explained as being due to the uncertainty in estimating its exact value due to the lower signal-to-noise ratio for increasing laser power. Nevertheless, the qualitative agreement between the experiment and the simulations seems to be acceptable, keeping in mind that the inclusion of the pump-beam focusing into the heat-pipe as described in Sect. 1, does not take into account the pump diffraction and also disregards diffraction of the waves generated in the nonlinear process. To obtain a more precise result, description by a coherently coupled system of four (2 + 1)-dimensional Schrödinger equations would be necessary, which to be solved would be a quite challenging problem.

In order to compare the weak and strong laser pumped regimes of the FWPM process we calculated the CE energy

density in dependence of angle. In Fig. 6, the dashed line refers to the yellow and the solid curve to the second, infrared CE (unfortunately, experimental data for this second CE are not available). At low pump intensities (up to 20% of the maximal value $I_1^{\max}$; see Figs. 3 and 4), both conical emissions appear at angles well predicted by (3a)–(3b). The weak asymmetry of the CEs toward smaller angles results from the asymmetric and variable overlapping between the yellow (infrared) and the laser waves (i.e. from the angularly-asymmetrical gain in dependence of conical emission "ring-centre").

The weak oscillations of different periods in the CE wings, which result from the higher side maxima in the phase-matching of the process [25], are also clearly seen in Fig. 6. The FWPM at high intensities was found to be insensitive to the particular noise-level assumed at the initiation stage of the process. When increasing the pump intensity the combined action of pump, SPM, and IPM leads to a spatial broadening of the yellow conical emission and to an increased overlapping of both CEs. The latter causes a local enhancement of process efficiency. The outer wing of the yellow CE becomes more amplified, whereas the same holds for the inner wing of the infrared CE.

In Fig. 7 we present the half-angles of the infrared (solid curve) and the yellow (dashed curve) CE in dependence of the pump-laser intensity at the laser wavelength $\lambda_{\mathrm{L}} = 330.13$ nm. The angle was associated with the centre of gravity of the emissions (cf. Fig. 5). From Fig. 7, one gets the impression, that both CEs "align" themselves while increasing the laser intensity (and therefore also the emission intensity). This behavior is due to the asymmetrical overlapping (and gain) and, although third order nonlinear susceptibilities are responsible, the behavior should be distinguished from the incoherent induced deflection of probe beams [26, 27].

Because we were not able to detect the spatial structure of the infrared conical emission (which behavior would give a direct experimental confirmation of the mechanism proposed), we tried to find other ways of confirmation. We calculated, using our model, the dependence of the yellow emission energy density on laser intensity (Fig. 8) and the yellow CE half-angle in dependence of the particle density
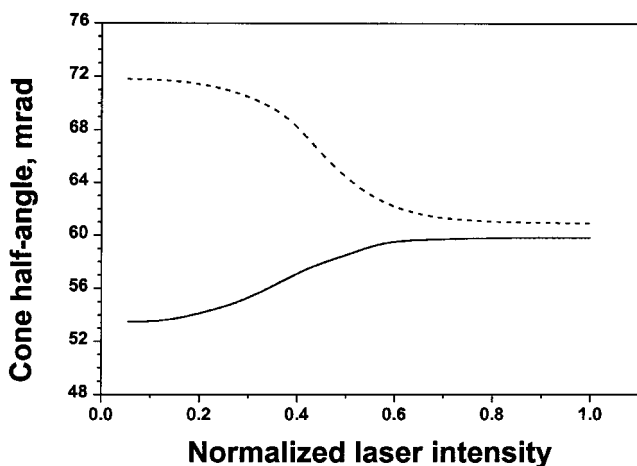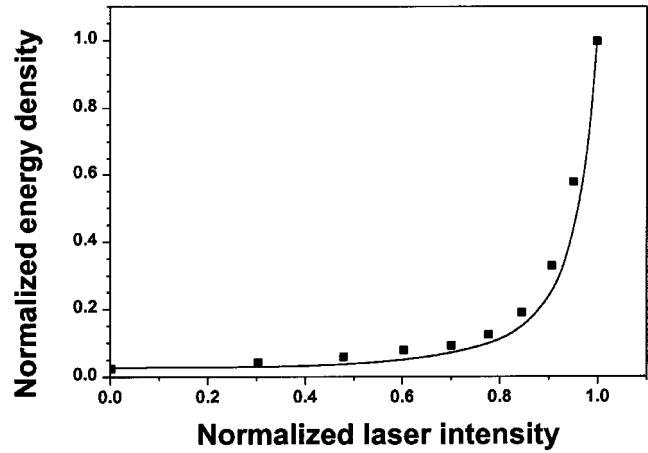

Fig. 8. Energy density of the yellow CE vs laser intensity. *Squares* experimental data; *solid curve* numerical result. $\lambda_{\mathrm{L}} = 330.13$ nm, $N = 1.6 \times 10^{17}$ cm^{-3}. Full laser intensity 2×10^9 W/cm^2
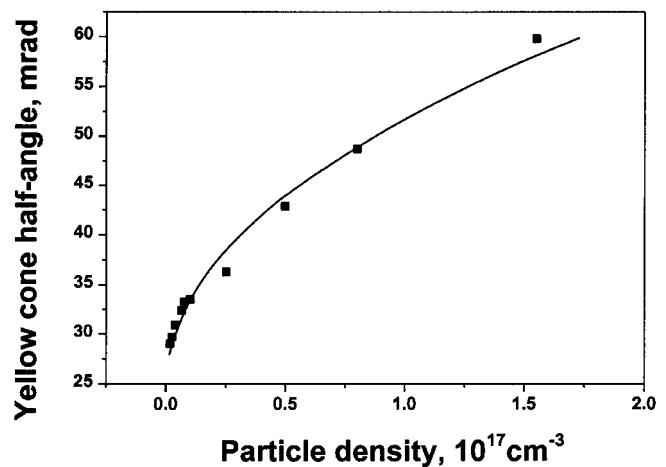

Fig. 9. Dependence of the yellow CE half-angle on the particle density at $\lambda_{\mathrm{L}} = 330.13$ nm. *Squares* experimental data; *solid* curve–numerical result

(Fig. 9). In both figures the solid lines indicate the numerical result, and the squares the experimental data obtained at $\lambda_{\mathrm{L}} = 330.13$ nm. One observes a fair agreement between theory and experiment. The strong nonlinearity of the CE energy density with laser intensity is a common effect within FWPM processes. From experimental data yellow CE angle was found to increase with $\sqrt{N}$ [1], which is also reproduced by the numerical model presented.

4 Conclusion

Following the simulation study we explain the increase and saturation behavior of the yellow CE angle observed by the mutual alignment between two conical emissions generated within our experiments. We proposed that the pump-induced phase modulation and asymmetric overlapping between the conical emissions generated in the FWPM process are responsible for the observed phenomena. The numerical results presented agree well with the experimental data. Qualitatively similar results were obtained under a plane-wave pump approximation at the expense of a decreased process-efficiency.

Fig. 7. Opposite angular tuning (*alignment*) between the yellow (*solid curve*) and infrared CE (*dashed*) at $\lambda_{\mathrm{L}} = 330.13$ nm, $N = 1.6 \times 10^{17}$ cm^{-3}

In a future experiment the simultaneous registration of the intensity behavior of both conical emissions could provide the proof for the explanation given in this work.

References

1. D.J. Harter, P. Naurum, M.G. Ramyer, R.W. Boyd: Phys. Rev. Lett. **46**, 1192 (1981)
2. A.C. Tam: Phys. Rev. A **19**, 1971 (1979)
3. M. LeBerre-Rousseau, E. Ressayre, A. Tallet: Opt. Comm. **36**, 31 (1981)
4. E.A. Chauchard, H.Y. Meyer: Opt. Comm. **52**, 141 (1984)
5. C.H. Skinner, P.D. Kleiber: Phys. Rev. A **21**, 151 (1980)
6. J.F. Valley, G. Khitrova, H.M. Gibbs, J.W. Grantham, J. Xu: Phys. Rev. Lett. **64**, 2362 (1990)
7. J. Pender, L. Hesselink: IEEE J. Quant. Electron. QE-**25**, 395 (1989)
8. H.Y. Meyer: Opt. Comm. **34**, 439 (1980)
9. G.G. Luther, A.C. Newell, J.V. Moloney, E.M. Wright: Opt. Lett. **19**, 789 (1994)
10. A. Gahl, J. Seipenbusch, A. Aumann, M. Möller, W. Lange: Phys. Rev. A **50**, R917 (1994)
11. J. Krasinsky, D.J. Gauthier, M.S. Malcuit, R.W. Boyd: Opt. Comm. **54**, 241 (1985)
12. C. Brechignac, Ph. Cahuac, A. Debarre: Opt. Comm. **52**, 141 (1980)
13. P.D. Kleiber, K. Burnet, J. Cooper: Phys. Rev. A **25**, 1188 (1982)
14. L. You, J. Mostowski, J. Cooper: Phys. Rev. A **46**, 2903 (1992) , Phys. Rev. A **46**, 2925 (1992)
15. T. Gustafson, J. Taran, H. Haus, T. Lifsitz, P. Kelley: Phys. Rev. **177**, 306 (1969)
16. R. Alfano, Q. Li, T. Jimbo, J. Manassah, P. Ho: Opt. Lett. **11**, 626 (1986)
17. M. Islam, L. Mollenaner, R. Stolen, J. Simpson, R. Shang: Opt. Lett. **6**, 129 (1981)
18. C. McKinstrie, D. Russel: Phys. Rev. Lett. **61**, 2929 (1988)
19. S. Dinev, A. Dreischuh: Opt. Quant. Electron. **23**, 91 (1991)
20. A. Dreischuh, V. Kamenov, S. Dinev, U. Reiter-Domiaty, D. Gruber, L. Windholz: J. Opt. Soc. Am. B (submitted)
21. S. Orlov, A. Yariv, M. Segev: Appl. Phys. Lett. **68**, 1610 (1996)
22. Y. Prior: IEEE J. Quant. Electron., QE-**20**, 27 (1984)
23. W.L. Wiese, M.W. Smith, B.M. Glennon: Atomic Transition Probabilities, vol II (NSRDS-NBS, Washington,1966)
24. W. Demtröder: Laser Spektroskopie, 3rd Ed., Chap. 2 (Springer Verlag, Berlin, Heidelberg, 1994)
25. J.F. Raintjes, Nonlinear Optical Parametric Processes in Liquids and Gases, Chap. 2 (Academic Press, Boston, 1984)
26. G.A. Swartzlander, Jr., H. Yin, A.E. Kaplan: J. Opt. Soc. Am., B **6**, 1317 (1989)
27. N. Goutev. A. Dreischuh, S. Baluschev, S. Dinev: IEEE J. Quant. Electron., QE-**31**, 2114 (1995)